Article

Comparison of Different Topologies of Thermal Management Subsystems in Multi-Stack Fuel Cell Systems

Wei Shen [1], Lei Fan [1,*], Zhirong Pan [2], Chunguang Chen [1], Ning Wang [1] and Su Zhou [1,2,*]

1   School of Automotive Studies, Tongji University, Shanghai 201804, China; ceo@tongji.edu.cn (W.S.);
    2031636@tongji.edu.cn (C.C.); wangning@tongji.edu.cn (N.W.)
2   Chinesisch-Deutsches Hochschulkolleg, Tongji University, Shanghai 201804, China; 2033604@tongji.edu.cn
*   Correspondence: kobebryant824@tongji.edu.cn (L.F.); suzhou@tongji.edu.cn (S.Z.)

Abstract: The performance of a fuel cell stack is affected by the operating temperature of the stack. The thermal management subsystem of a multi-stack fuel cell system (MFCS) is particularly significant for the operating temperature control of each stack in the MFCS. To study the influence of different topologies of a MFCS thermal management subsystem, this paper proposes and establishes two different topologies. Firstly, the integrated topology is proposed. Secondly, seven component models, namely the mixer, thermostat, radiator, tank, pump, bypass value, and proton exchange membrane fuel cell stack temperature models, are described in detail. Finally, the performance of the two topologies of the MFCS thermal management subsystem under two working conditions, steady (200 A) and variable (China heavy-duty commercial test cycle, C-WTVC), is compared. Furthermore, there are two evaluating indicators, including the stability duration and deviation of the operating temperatures of the single stack in the MFCS. Results show that when the MFCS operates under steady working conditions, the integrated topology is superior in operating temperature control accuracy ($\Delta T < 0.5$ K), while the distributed topology is superior in the adjustment process (t $\leq$ 100 s). Moreover, when the MFCS operates under variable working conditions, the distributed topology is superior in operating temperature control accuracy.

Keywords: MFCS; thermal management subsystem; operating temperature; topology

1. Introduction

Due to environmental protection and greenhouse gas emissions, the development of new energy resources is becoming a significant measure for governments [1]. Among them, hydrogen energy is a promising candidate because it has zero emissions, high power density, and a wide variety of sources [2]. The fuel cell system using hydrogen energy is developing rapidly [3]. However, with the enrichment of application scenarios for fuel cell systems, the requirement for its power level is becoming higher and higher [4,5]. It is difficult for a single fuel cell stack to meet the requirement because of uniformity, cost, and technology issues [5]. The multi-stack fuel cell system (MFCS) can solve these issues, and it has several advantages such as immense power, high efficiency, and a long lifespan [6]. It is widely known that the operating temperature is important to the fuel cell system because it determines the performance and normal operation of the fuel cell system [7]. In the MFCS, the thermal subsystem plays a significant role in controlling the operating temperature. Therefore, it is necessary to study the thermal subsystem of the MFCS. It is noted that the thermal management subsystem consisting of seven component models is applied to control the operating temperature of each stack in the MFCS. Each component has its function. For example, the mixer model is applied to filter different outlet coolant temperatures of the multi-stack into a temperature. The thermostat model is applied to control the large and small cycles of the coolant. The radiator model is applied to calculate the heat dissipation. The tank model is applied to store the coolant. The pump model is

applied to provide the flow rate of the coolant. The bypass value model is applied to control the coolant flow rate of each stack. The proton exchange membrane fuel cell (PEMFC) stack temperature model is applied to calculate the stack heat production.

Unfortunately, there are few works about the thermal subsystem of the MFCS because of few MFCS applications [5]. In our opinion, there are four aspects of thermal subsystem research: topology, architecture, component selection, and control algorithm/strategy. For thermal subsystem topology, there are two topologies: distributed and integrated. Wu et al. [8] showed an actual 65 kW dual-stack PEMFC system, which arranges a parallel coolant pipeline. The thermal subsystem is used by the integrated topology. Moreover, the architecture is determined after the determination of the topology. For the thermal subsystem architecture, Dépature et al. [9] proposed the series- and parallel-type architectures and pointed out the advantages and disadvantages of the two architectures. In the series type, the coolant flows to each stack in sequence. In the parallel type, the coolant flows to each stack at the same time. It is noted that the integrated topology was used in two architectures of their work. For the component selection, the thermal subsystem components of the MFCS are similar to those of the single fuel cell stack. Therefore, the component selection can be conducted according to specific requirements. For the control algorithm/strategy, Mohamed et al. [10] proposed a thermal management control algorithm to control the operating temperature of each stack in the MFCS. In their algorithm, the excess heat quantity produced by the operating stack could preheat the next stack. There are three benefits, namely shortening the startup time of the next stack, saving energy, and improving the MFCS response. Furthermore, de Bortoli et al. [11] proposed a thermal management strategy to minimize the startup, heating/cooling, and cycling issues inside the EV. Results show that the appropriate thermal management strategy is helpful to improve the life span, cycling, and efficiency of the MFCS.

This paper fills the modeling gap of the MFCS thermal subsystem. It designs, models, and compares two different topologies of the MFCS. Firstly, two different topologies, distributed and integrated, are proposed. On the one hand, the distributed topology consists of three independent thermal management subsystems. On the other hand, the integrated topology consists of only one thermal management subsystem. Secondly, seven component models, namely the mixer, thermostat, radiator, tank, pump, bypass value, and PEMFC stack temperature, are described in detail. Finally, the performance of the two topologies of the MFCS thermal management subsystem under two working conditions, steady and variable, is compared.

2. Topology of the MFCS Thermal Management Subsystem

Depending on whether it is integrated or not, there are two topologies of the MFCS thermal management subsystem. In this paper, the MFCS consists of three stacks, and detailed topologies are shown in Figure 1a,b. On the one hand, the distributed topology consists of three independent thermal management subsystems. On the other hand, the integrated topology consists of only one thermal management subsystem. The advantages and disadvantages of the two topologies are shown in Table 1. Moreover, the thermal management subsystem includes several components, such as the tank, pump, deionizer, thermostat, and radiator.
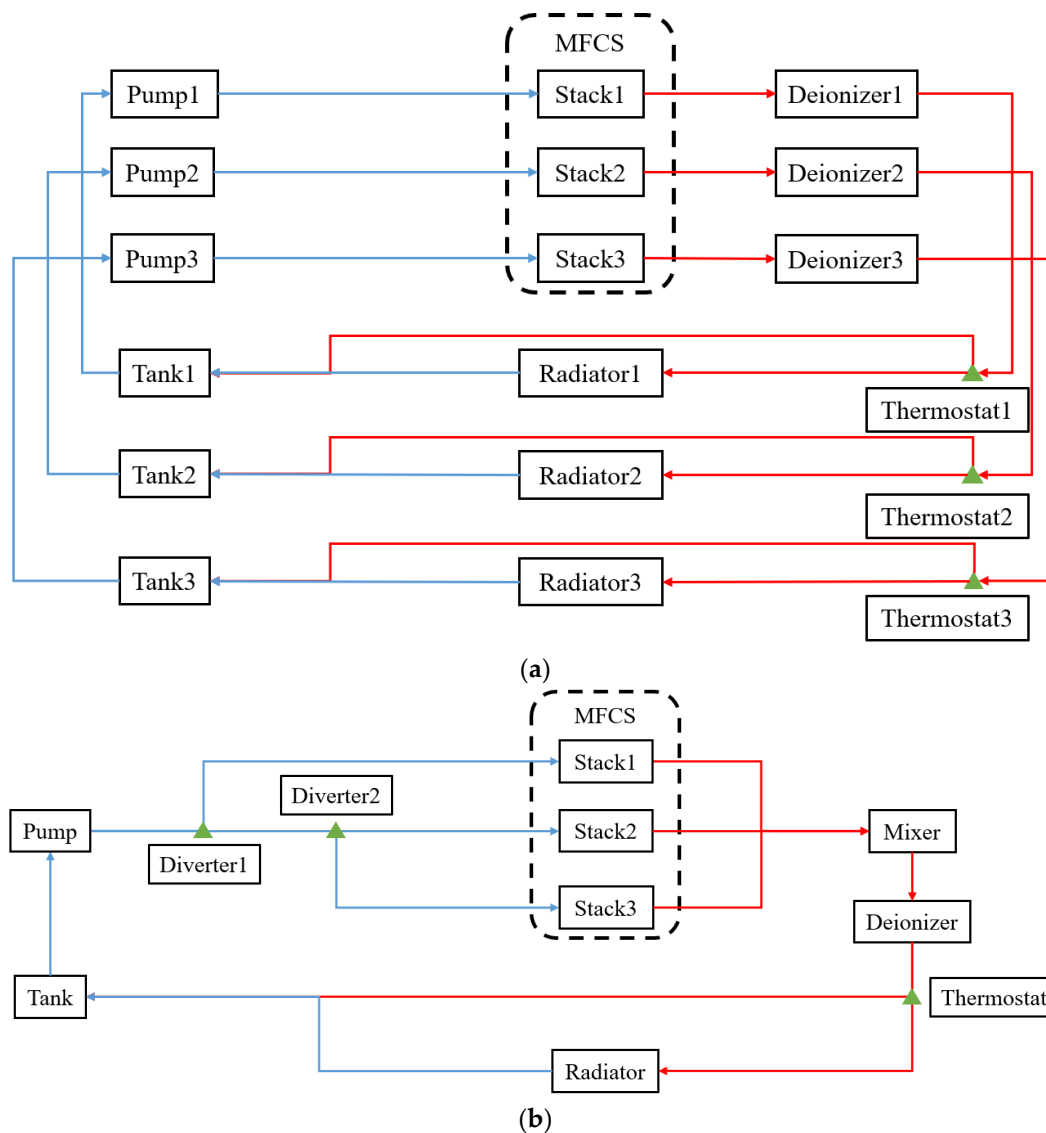
Figure 1. Topologies of the MFCS thermal management subsystem: (**a**) distributed and (**b**) integrated.

Table 1. The advantages and disadvantages of the two topologies.

	Advantages	Disadvantages
Distributed topology	Independently controls each stack operating temperature	A large number of components, high cost
Integrated topology	A small number of components, low cost	The operating temperature of each stack interferes with the others

3. Component Models of the MFCS Thermal Management Subsystem

This section describes the main seven component models: the mixer, thermostat, radiator, tank, pump, bypass value, and PEMFC stack temperature models.

3.1. Mixer Model

The mixer model consists of two parts: the flow rate and temperature. The coolant flow rate of the mixer outlet can be represented in the form below:

$$W_{\text{co\_mixer\_out}} = \sum_{i=1}^{3} W_{\text{co\_st}(i)\_\text{out}} \tag{1}$$

where $W_{\text{co\_mixer\_out}}$ is the coolant flow rate of the mixer outlet, kg/s; $W_{\text{co\_st}(i)\_\text{out}}$ is the coolant flow rate of the *i*th stack outlet, kg/s, *i* = 1, 2, 3.

It is assumed that the mixer does not exchange heat with the environment, so only the heat exchange between coolants with different temperatures occurs inside the mixer. The coolant temperature of the mixer outlet can be represented in the form below:

$$T_{\text{co\_mixer\_out}} = \frac{\sum_{i=1}^{3} W_{\text{co\_st}(i)\_\text{out}} T_{\text{co\_st}(i)\_\text{out}}}{\sum_{i=1}^{3} W_{\text{co\_st}(i)\_\text{out}}} \tag{2}$$

where $T_{\text{co\_mixer\_out}}$ is the coolant temperature of the mixer outlet, K; $T_{\text{co\_st}(i)\_\text{out}}$ is the coolant temperature of the *i*th stack outlet, K, *i* = 1, 2, 3.

It is noted that the coolant temperature change is described by the first-order inertia link. The time constant can be determined by the experiment or experience. Moreover, it determines the stability time of the coolant temperature. In this paper, the time constant is set to 0.5 s.

The input and output and the Simulink model of the mixer are shown in Figures 2 and 3. The input of the mixer includes flow rates and temperatures of the three stacks' coolants (Co_ includes the flow rate and the temperature of the coolant), and the output includes the flow rate and temperature of the mixer outlet.
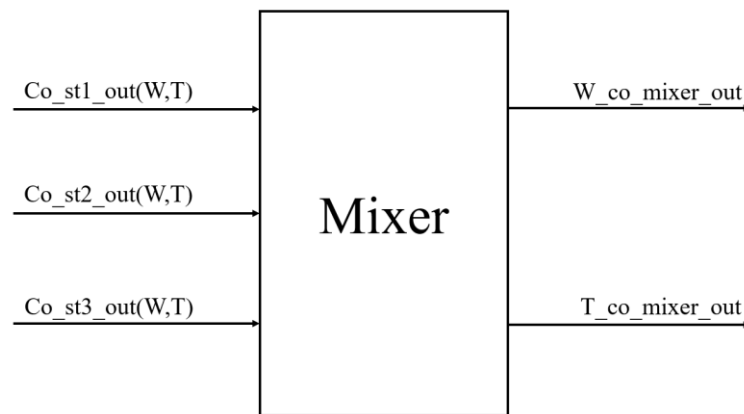
Figure 2. The input and output of the mixer model.
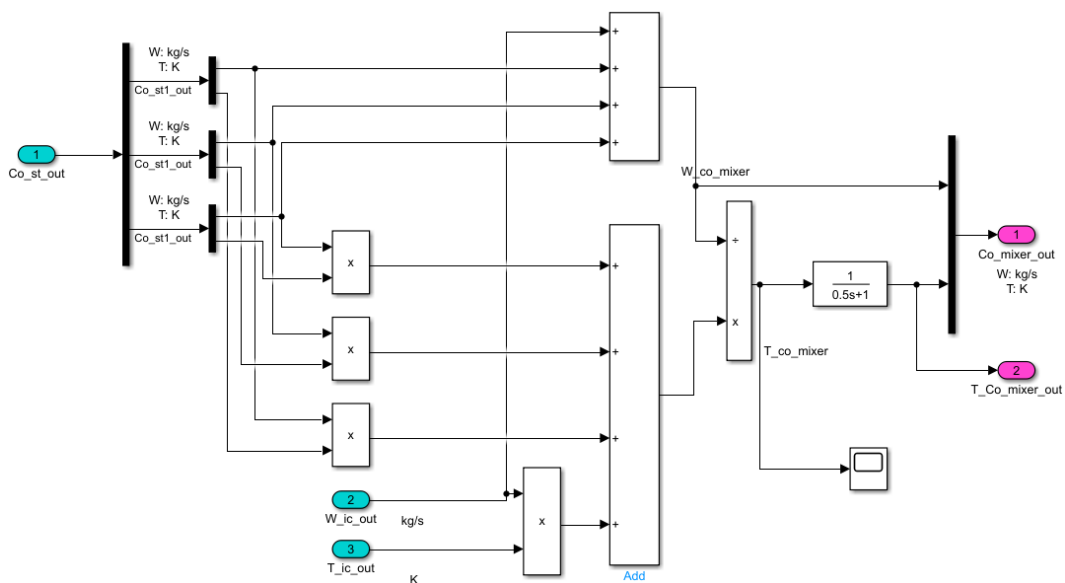
Figure 3. The Simulink model of the mixer.

3.2. Thermostat Model

The thermostat model also consists of two parts: the flow rate and temperature. The coolant flow rate and temperature of the thermostat inlet can be represented in the form below:

$$T_{co\_thermostat\_in} = T_{co\_mixer\_out} \tag{3}$$

$$W_{co\_thermostat\_in} = W_{co\_mixer\_out} \tag{4}$$

where $T_{co\_thermostat\_in}$ is the coolant temperature of the thermostat inlet, K; $W_{co\_thermostat\_in}$ is the coolant flow rate of the thermostat inlet, kg/s.

The opening of the thermostat determines the proportion of the coolant flow rates of the big and small loops:

$$W_{co\_big} = W_{co\_thermostat\_in} \cdot Phi\_bypass\_big \tag{5}$$

$$W_{co\_small} = W_{co\_thermostat\_in} \cdot (1 - Phi\_bypass\_big) \tag{6}$$

where W_{co_big} is the coolant flow rate of the big loop, kg/s; Phi_bypass_big is the opening of the thermostat; W_{co_small} is the coolant flow rate of the small loop, kg/s.

It is assumed that the thermostat does not exchange heat with the environment, so only the heat exchange between coolants with different temperatures occurs in the thermostat. The coolant temperature of the thermostat outlet can be represented in the form below:

$$T_{co\_big} = T_{co\_thermostat\_in} \tag{7}$$

$$T_{co\_small} = T_{co\_thermostat\_in} \tag{8}$$

where T_{co_big} and T_{co_small} are coolant temperatures of the big and small loop, respectively, K.

The input and output and the Simulink model of the thermostat are shown in Figures 4 and 5. The input of the thermostat includes the opening of the thermostat, coolant flow rate, and temperature of the thermostat inlet, and the output includes flow rates and temperatures of the big and small loops.
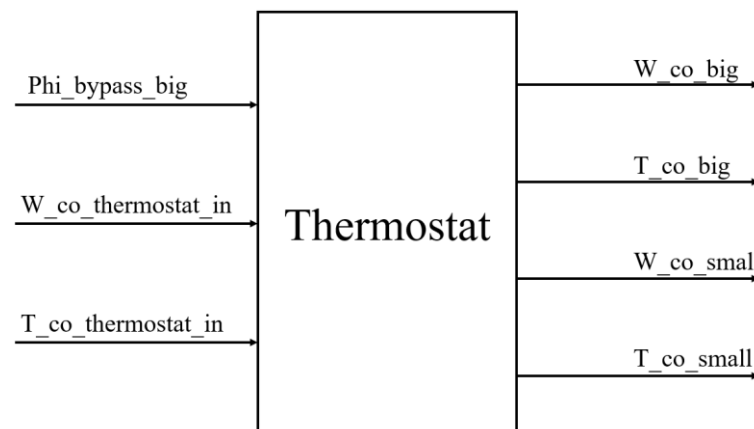
Figure 4. The input and output of the thermostat model.
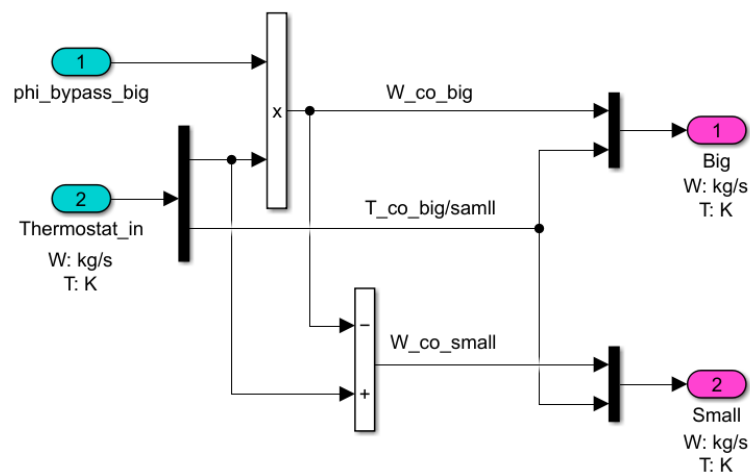
Figure 5. The Simulink model of the thermostat.

3.3. Radiator Model

The flow rate of the radiator is equal to that of the big loop, and it can be represented in the form below:

$$W_{\text{co\_rad\_out}} = W_{\text{co\_big}} \tag{9}$$

The cooling capacity of the radiator is affected by its surface wind speed, heat dissipation area, ambient temperature, and installation position. Moreover, the surface wind speed is determined by vehicle and fan speeds and measured by the experiment. The relationship between the surface wind speed and vehicle and fan speeds obtained by the experimental data fitting can be represented in the form below:

$$v_w = 0.1568 + 0.0015846 \times n_{\text{fan}} + 0.02233 \times v \tag{10}$$

where v_w is the surface wind speed, m/s; n_{fan} is the fan speed, rpm; v is the vehicle speed, km/h.

When the ambient temperature and the radiator size are determined, the cooling capacity is determined by the surface wind speed and coolant flow rate, and the relationship can also be measured by the experiment. The LUT$\left(W_{\text{co\_big}}, v_{\text{wind}}\right)$ applied in this model is shown in Figure 6.
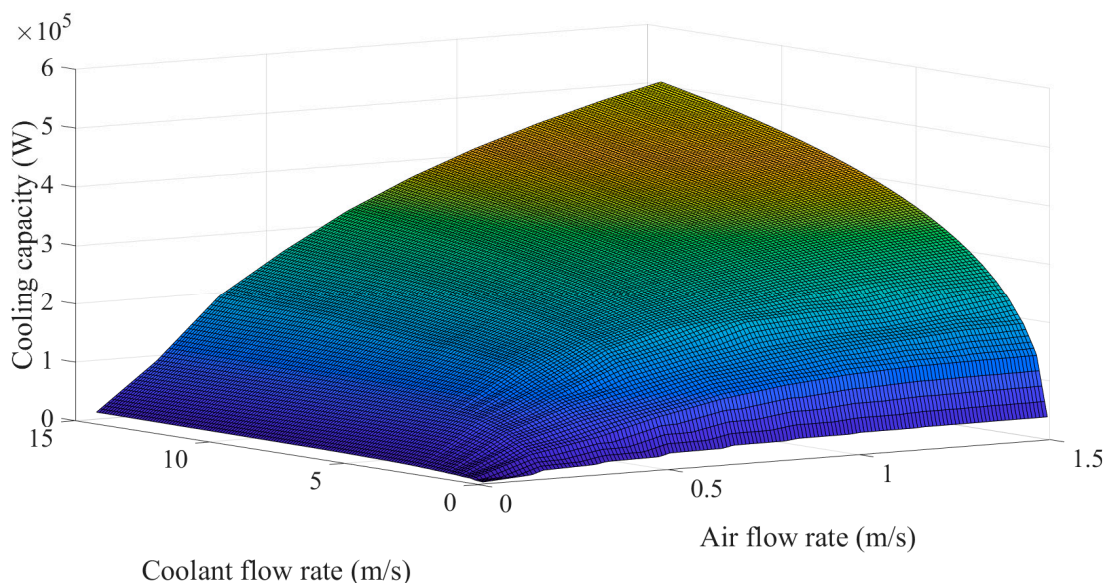
Figure 6. The LUT of the radiator.

The above relationship is obtained when the temperature difference between the coolant inlet and ambient temperature is 60 K. Moreover, the modified relationship is represented in the form below when the ambient temperature is changing:

$$\dot{Q}_{\text{rad\_rel}} = \dot{Q}_{\text{rad\_exp}} \left(\frac{T_{\text{co\_big}} - T_{\text{amb}}}{60} \right) \tag{11}$$

where $\dot{Q}_{\text{rad\_rel}}$ is the real cooling capacity of the radiator, kW; $\dot{Q}_{\text{rad\_exp}}$ is the theoretical cooling capacity of the radiator, kW; T_{amb} is the ambient temperature, K.

According to the heat transfer equation, the coolant temperature of the radiator outlet is represented in the form below:

$$\dot{T}_{\text{co\_rad\_out}} = \frac{C_{\text{co}} W_{\text{co\_rad\_out}} \left(T_{\text{co\_big}} - T_{\text{co\_rad\_out}} \right) - \dot{Q}_{\text{rad\_rel}}}{m_{\text{co\_rad}} W_{\text{co\_rad\_out}}} \tag{12}$$

where $\dot{T}_{\text{co\_rad\_out}}$ is the coolant temperature change rate of the radiator outlet, K/s; C_{co} is the specific heat capacity, J/(kg·K); $T_{\text{co\_rad\_out}}$ is the coolant temperature of the radiator outlet, K; $m_{\text{co\_rad}}$ is the coolant mass inside the radiator, kg.

The input and output and the Simulink model of the radiator are shown in Figures 7 and 8. The input of the radiator includes the fan speed, vehicle speed, coolant flow rate and temperature of the big loop, and ambient temperature. In addition, the output includes the coolant flow rate and temperature of the radiator outlet.
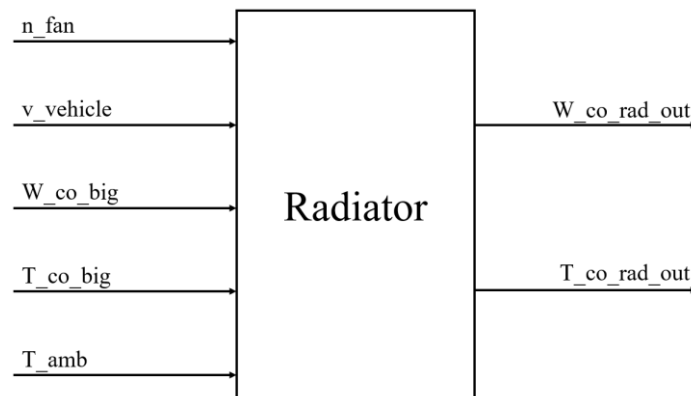
Figure 7. The input and output of the radiator model.
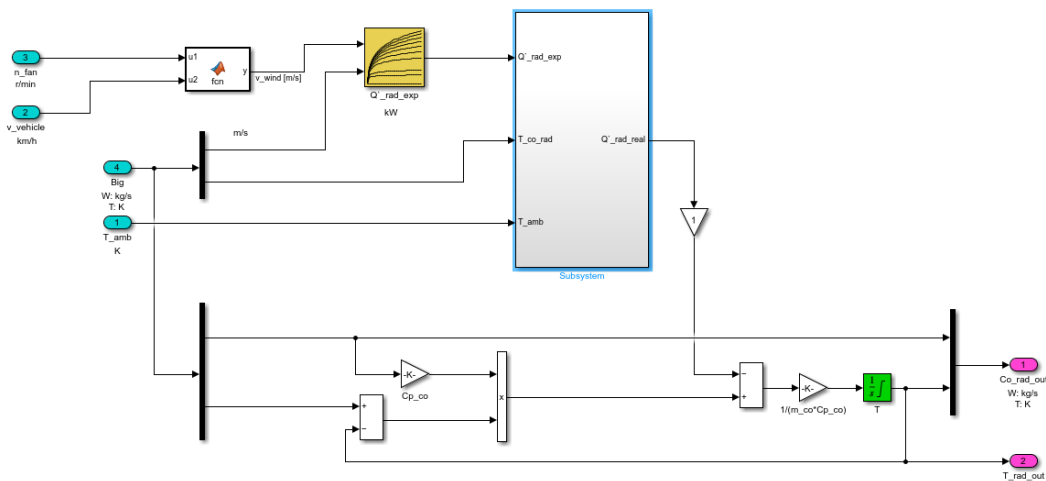
Figure 8. The Simulink model of the radiator.

3.4. Tank and Pump Model

The temperature of the tank outlet is determined by the coolant states of the radiator outlet, small loop, and the remaining coolant in the tank, and it can be represented in the form below:

$$T_{\mathrm{co\_tank\_out}} = \frac{W_{\mathrm{co\_rad\_out}}T_{\mathrm{co\_rad\_out}} + W_{\mathrm{co\_small}}T_{\mathrm{co\_small}} + W_{\mathrm{co\_tank}}T_{\mathrm{co\_tank\_out}}}{W_{\mathrm{co\_rad\_out}} + W_{\mathrm{co\_small}} + W_{\mathrm{co\_tank}}} \qquad (13)$$

where $T_{\mathrm{co\_tank\_out}}$ is the temperature of the tank outlet, K; $W_{\mathrm{co\_rad\_out}}$ is the coolant flow rate of the radiator outlet, kg/s; $W_{\mathrm{co\_small}}$ is the coolant flow rate of the small loop, kg/s; $W_{\mathrm{co\_tank}}$ is the coolant flow rate of the remaining coolant in the tank, kg/s; $T_{\mathrm{co\_rad\_out}}$ is the coolant temperature of the radiator outlet, K; $T_{\mathrm{co\_small}}$ is the coolant temperature of the small loop, K.

The coolant flow rate of the tank outlet is determined by the pump and can be represented in the form below:

$$W_{\mathrm{co\_rad\_out}} = W_{\mathrm{co\_pump\_out}} \qquad (14)$$

where $W_{\mathrm{co\_pump\_out}}$ is the coolant flow rate of the pump outlet, kg/s.

The input and output and the Simulink model of the tank and pump are shown in Figures 9 and 10. The input of the tank and pump includes the coolant flow rates and temperatures of the radiator outlet and small loop. Additionally, the output includes the coolant flow rate and temperature of the tank outlet.
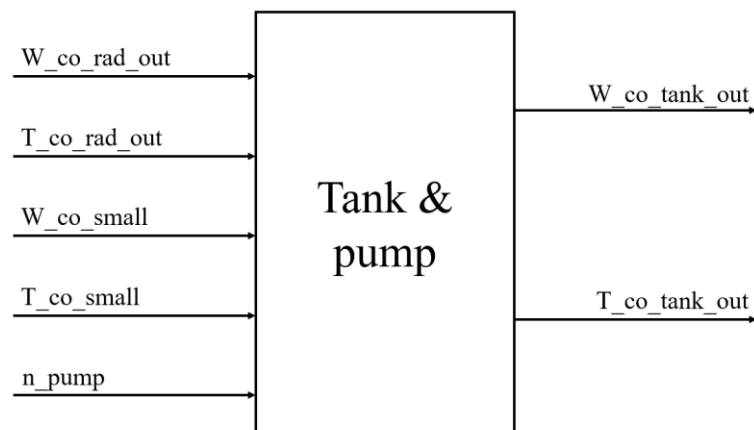
Figure 9. The input and output of the tank and pump model.
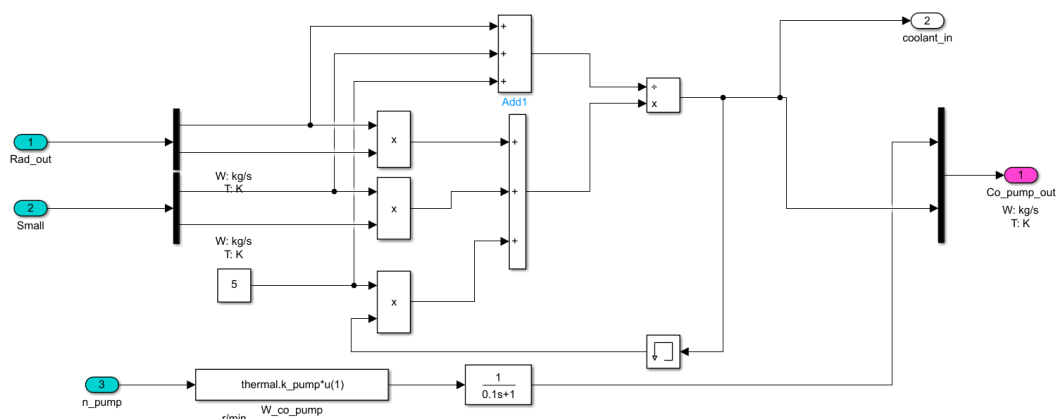
Figure 10. The Simulink model of the tank and pump.

3.5. Bypass Value Model

Coolant flow rates of different loops are determined by the coolant flow rate and opening of the bypass:

$$W_{co\_1} = W_{co\_bypass\_in} \cdot Phi_{bypass} \tag{15}$$

$$W_{co\_2} = W_{co\_bypass\_in} \left(1 - Phi_{bypass}\right) \tag{16}$$

where W_{co_i} is the coolant flow rate flowing to the ith stack, kg/s; $W_{co\_bypass\_in}$ is the coolant flow rate flowing to the bypass, kg/s; Phi_{bypass} is the bypass opening.

It is assumed that the temperature flowing to the bypass is not changed:

$$T_{co\_1} = T_{co\_2} = T_{co\_bypass\_in} \tag{17}$$

where T_{co_i} is the temperature flowing to the ith stack, K; $T_{co\_bypass\_in}$ is the temperature flowing to the bypass, K.

The input and outputand the Simulink model of the bypass are shown in Figures 11 and 12. The input of the bypass includes the bypass opening, coolant flow rate and temperature of the bypass inlet. In addition, the output includes the coolant flow rates and temperatures of different loops.
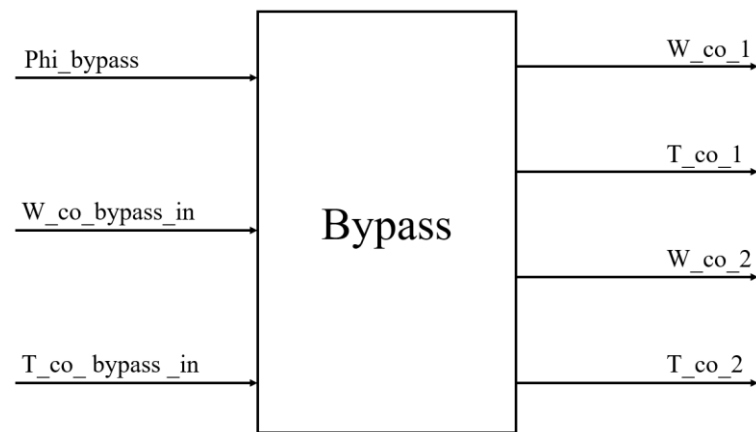
Figure 11. The input and output of the bypass model.
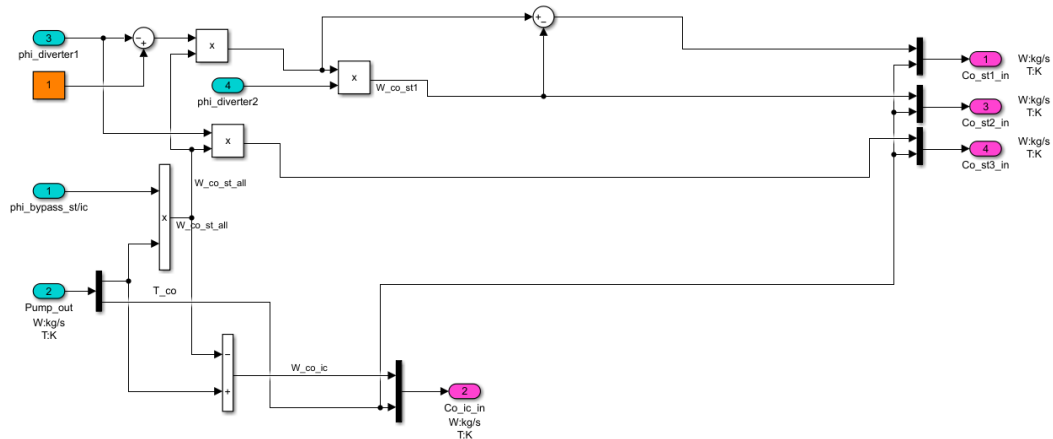
Figure 12. The Simulink model of the bypass.

3.6. PEMFC Stack Temperature Model

The PEMFC stack temperature is determined by four parts: the stack heat generation, natural convection, radiation convection, and force convection (radiator heat dissipation):

$$\dot{Q}_{st} = \dot{Q}_{add} - \dot{Q}_{conv\_nat} - \dot{Q}_{conv\_rad} - \dot{Q}_{conv\_force} \tag{18}$$

where $\dot{Q}_{st}$ is the stack heat change, W; $\dot{Q}_{add}$ is the stack heat generation, W; $\dot{Q}_{conv\_nat}$ is the natural convection, W; $\dot{Q}_{conv\_rad}$ is the radiation convection, W; $\dot{Q}_{conv\_force}$ is the forced convection, W.

$$\dot{Q}_{st} = C_{st} m_{st} \frac{dT_{st}}{dt} \tag{19}$$

$$\dot{Q}_{add} = (n_{cell} E_{nernst} - V_{st}) I_{st} + (\dot{Q}_{in} - \dot{Q}_{out})_{react} \tag{20}$$

$$\dot{Q}_{conv\_rad} = A_{st\_exterior} \times 0.85 \times 5.67 \times 10^{-8} \times \left(T_{st}^4 - T_{amb}^4\right) \tag{21}$$

$$\dot{Q}_{conv\_nat} = h_{st} A_{st\_exterior}(T_{st} - T_{amb}) \tag{22}$$

$$\dot{Q}_{conv\_force} = C_{co} W_{co\_st\_in}(T_{st} - T_{co\_st\_in}) \tag{23}$$

where:

$$\begin{aligned}
\dot{Q}_{in} = \ & Cp_{O_2} W_{O_2\_in}(T_{ca\_in} - T_{amb}) + Cp_{N_2} W_{N_2\_ca\_in}(T_{ca\_in} - T_{amb}) + Cp_{N_2} W_{N_2\_an\_in}(T_{an\_in} - T_{amb}) \\
& + Cp_{H_2} W_{H_2\_in}(T_{an\_in} - T_{amb}) + Cp_{vap} W_{vap\_ca\_in}(T_{ca\_in} - T_{amb}) \\
& + Cp_{vap} W_{vap\_an\_in}(T_{an\_in} - T_{amb})
\end{aligned} \tag{24}$$

$$\begin{aligned}
\dot{Q}_{out} = \ & Cp_{O_2} W_{O_2\_out}(T_{ca\_out} - T_{amb}) + Cp_{N_2} W_{N_2\_ca\_out}(T_{ca\_out} - T_{amb}) + Cp_{N_2} W_{N_2\_an\_out}(T_{an\_out} - T_{amb}) \\
& + Cp_{H_2} W_{H_2\_out}(T_{an\_out} - T_{amb}) + Cp_{vap} W_{vap\_ca\_out}(T_{ca\_out} - T_{amb}) \\
& + Cp_{vap} W_{vap\_an\_out}(T_{an\_out} - T_{amb})
\end{aligned} \tag{25}$$

where C_{st} is the stack-specific heat capacity, J/(kg·K); m_{st} is the stack mass, kg; T_{st} is the stack temperature, K; n_{cell} is the number of the single fuel cell in the stack; E_{nernst} is Nernst voltage, V; V_{st} is the stack voltage, V; $A_{st\_exterior}$ is the external surface area of the stack, m^2; T_{amb} is the ambient temperature, K; h_{st} is the convective heat transfer coefficient, W/(m^2·K); C_{co} is the coolant-specific heat capacity, J/(kg·K); $T_{co\_st\_in}$ is the coolant temperature of the stack inlet, K; Cp_{O_2} is the O$_2$-specific heat capacity, J/(kg·K); Cp_{N_2} is the N$_2$-specific heat capacity, J/(kg·K); Cp_{H_2} is the H$_2$-specific heat capacity, J/(kg·K); Cp_{vap} is the vapor-specific heat capacity, J/(kg·K); T_{ca_in} is the cathode inlet temperature, K; T_{an_in} is the anode inlet temperature, K; $W_{N_2\_ca\_in}$ is the N$_2$ flow rate of the cathode inlet, kg/s; $W_{O_2\_in}$ is the O$_2$ flow rate of the cathode inlet, kg/s; $W_{vap\_ca\_in}$ is the vapor flow rate of the cathode inlet, kg/s; $W_{N_2\_an\_in}$ is the N$_2$ flow rate of the anode inlet, kg/s; $W_{H_2\_in}$ is the H$_2$ flow rate of the anode inlet, kg/s; T_{ca_out} is the cathode outlet temperature, K; T_{an_out} is the anode outlet temperature, K; $W_{N_2\_ca\_out}$ is the N$_2$ flow rate of the cathode outlet, kg/s; $W_{O_2\_out}$ is the O$_2$ flow rate of the cathode outlet, kg/s; $W_{vap\_ca\_out}$ is the vapor flow rate of the cathode outlet, kg/s; $W_{N_2\_an\_out}$ is the N$_2$ flow rate of the anode outlet, kg/s; $W_{H_2\_out}$ is the H$_2$ flow rate of the anode outlet, kg/s.

The input and outputand the Simulink model of the stack temperature are shown in Figures 13 and 14. The input of the stack temperature includes the current, voltage of the stack, H$_2$, O$_2$, N$_2$ and vapor flow rates of the inlet and outlet, coolant flow rate of the stack inlet, reacant temperatures of the inlet and outlet, ambient temperature, and coolant temperature rate of the stack inlet. In addition, the output includes the stack temperature, coolant flow rate and temperature of the stack outlet.
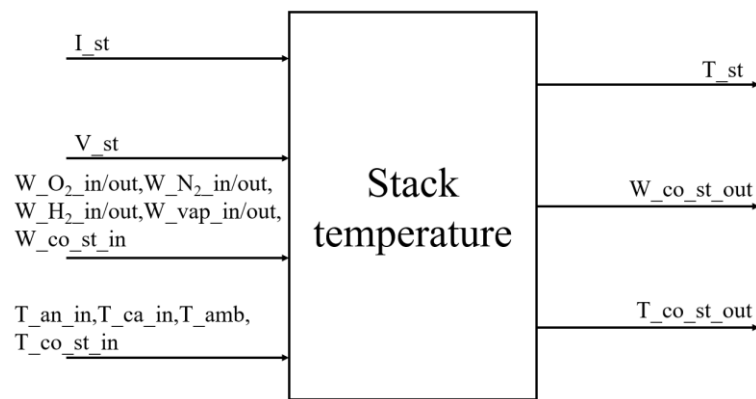
Figure 13. The input and output of the stack temperature model.
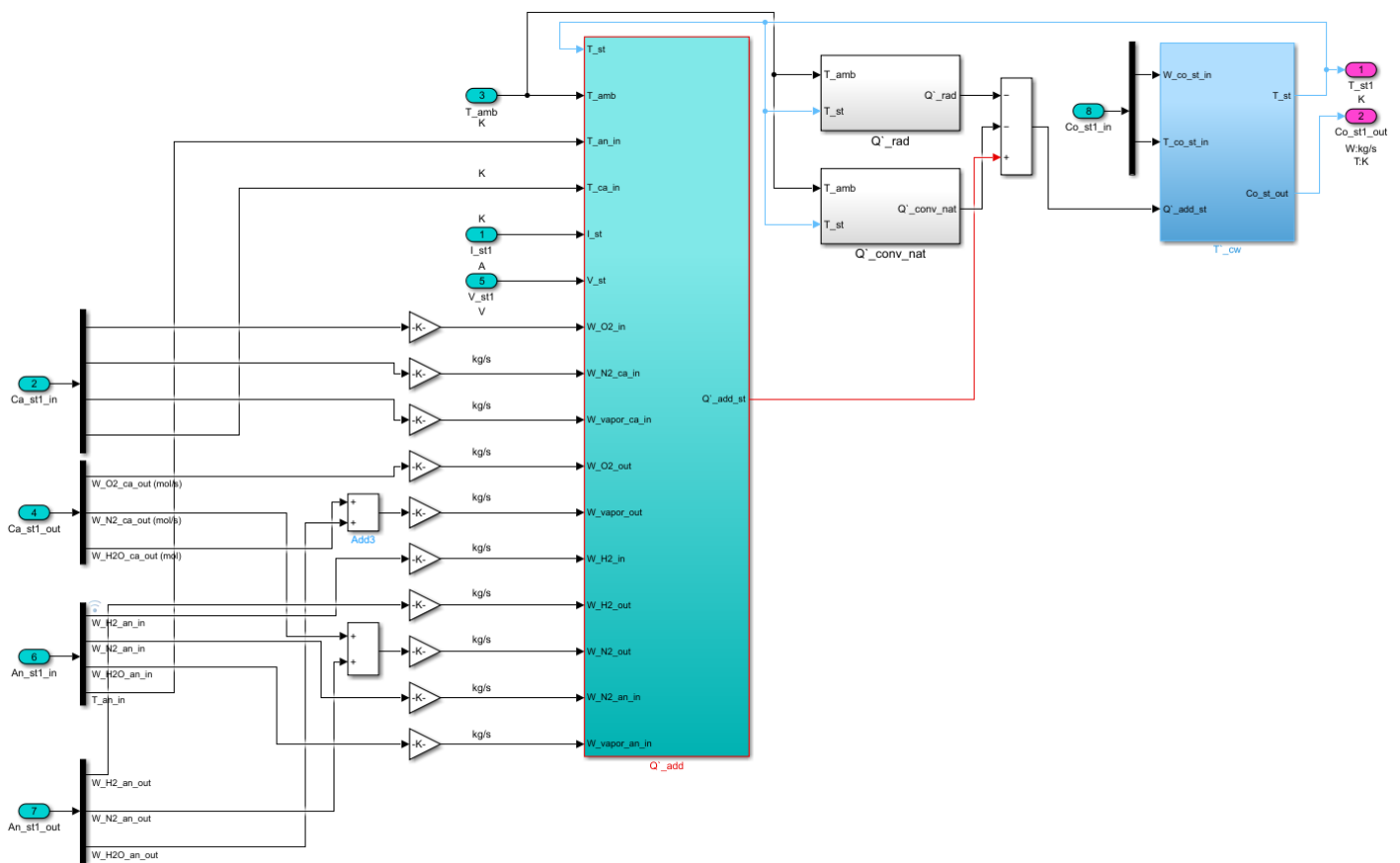
Figure 14. The Simulink model of the stack temperature.

4. Results and Discussion

This section compares the performance of the two topologies of the MFCS thermal management subsystem under two working conditions: steady and variable. Steady (200 A) and variable (China heavy-duty commercial test cycle, C-WTVC) working conditions are shown in Figure 15a,b. There are two evaluating indicators: the stability duration and deviation of the operating temperatures of the single stack in the MFCS. It is noted that for the evaluation index of the thermal management, besides stability duration and deviation of the operating temperatures, there are also the power consumption and life of the thermal management subsystem. However, in the whole MFCS, the power consumption of the thermal management subsystem accounts for only less than 1% of the power provided by the MFCS, while the power consumption of the compressor (supply air) accounts for 10~20% of the power provided by the MFCS. Therefore, the power consumption of

the thermal management is negligible. Moreover, the life of the thermal management subsystem is much longer than that of the MFCS. So, the life of the thermal management subsystem is also negligible.

(a)

(b)
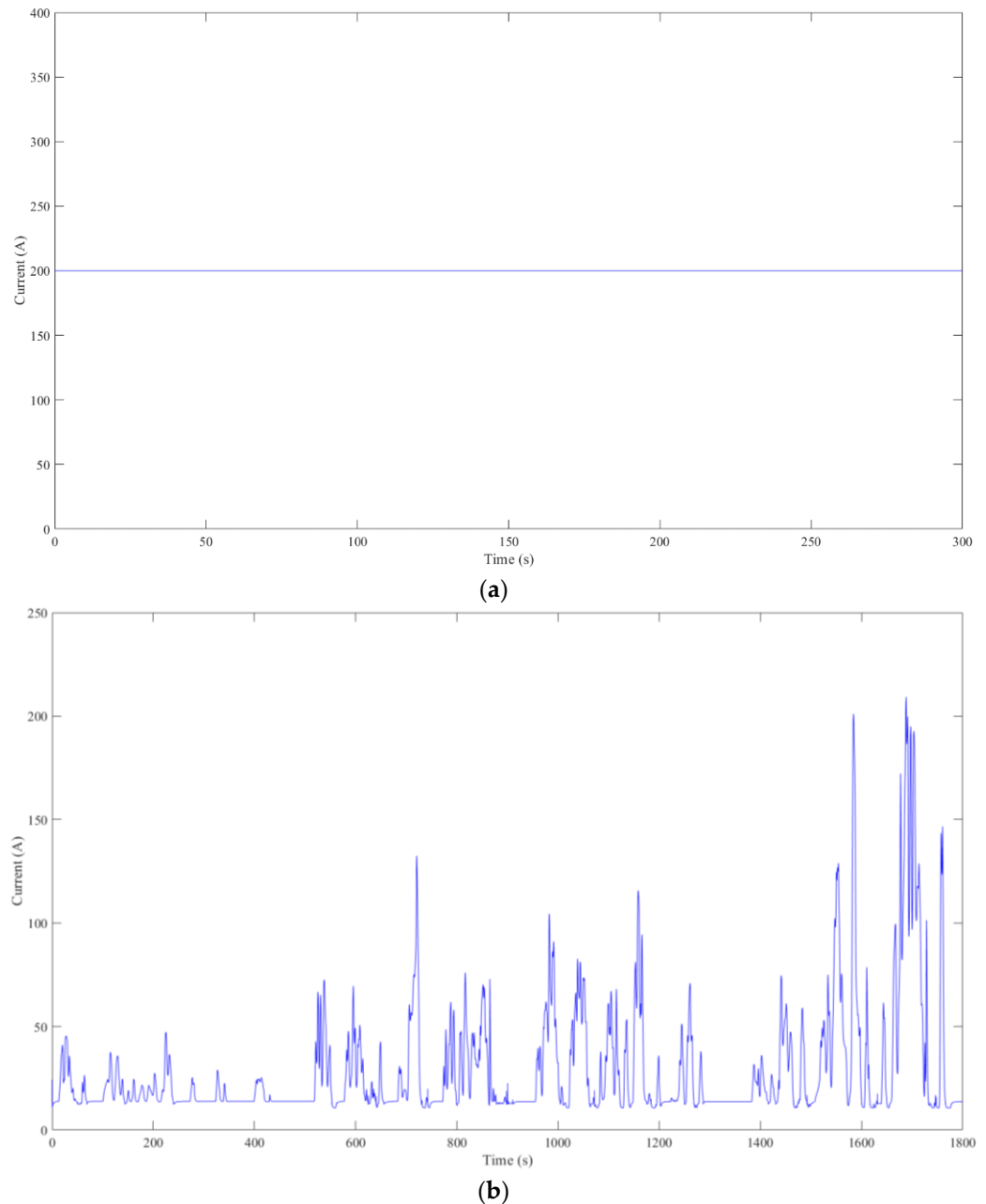
Figure 15. Two working conditions: (**a**) steady working conditions and (**b**) variable working conditions.

4.1. Steady Working Conditions

The three stacks' temperatures of the two topologies when the MFCS operates under steady working conditions are shown in Figure 16a,b. On the one hand, the temperature overshoot of the distributed topology is large, and the operating temperature of this topology has a steady-state error. However, its advantage is the short stabilization time. Moreover, the temperature overshoot of three stacks is $T_{st3} > T_{st2} > T_{st1}$. The possible reason is that the temperature has characteristics of a strong time delay and slow response, and the heat transfer process is related to the quality of the stack ($m_{st3} > m_{st2} > m_{st1}$). The reason for the steady-state error of the operating temperature is that the component selection is not completely matched due to the parameters of components. The stabilization

time of the three stacks is the same because the thermal subsystem of each stack in this topology is independent of the others, and the temperature of each stack has no interference with the others. This is also the biggest advantage of this topology. On the other hand, the temperature overshoot of the integrated topology is minimal. However, it needs a long stabilization time. The reason is that the three stacks interfere with each other. Moreover, the temperature overshoot of the three stacks is $T_{st2} > T_{st3} > T_{st1}$. The reason is that the coolant flow rate change of stack 2 is severe because it is at the intersection of two coolant flows. It is noted that the operating temperature adjustment of the integrated topology needs a longer time than that of the distributed topology because the coolant flow rates of the three stacks interfere with each other.

(a)

(b)
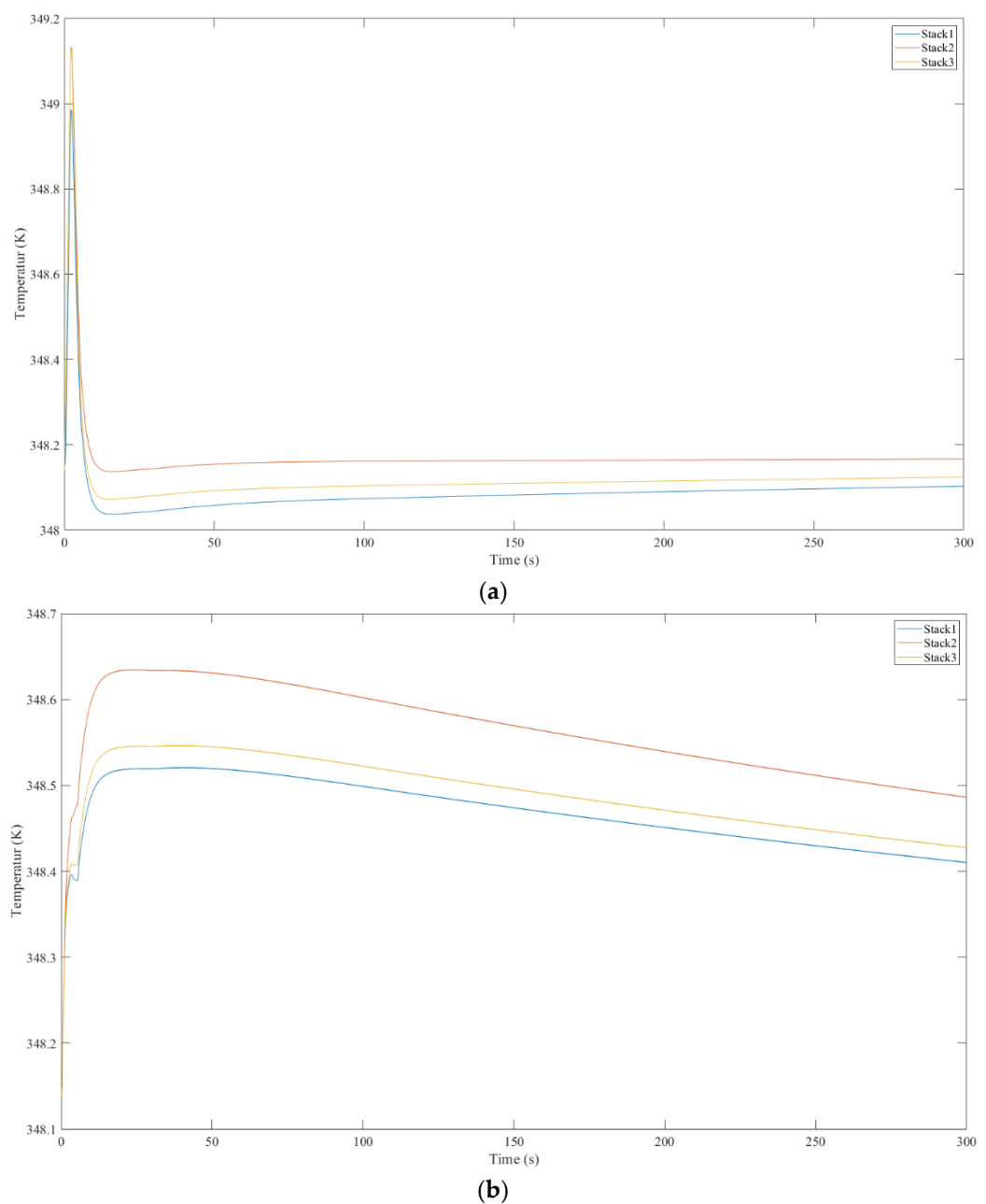
Figure 16. Three stacks' temperatures of the two topologies under steady working conditions: (**a**) distributed topology and (**b**) integrated topology.

In this paper, the desired operating temperature is 348.15 K. The temperature overshoot is defined as the difference between the actual maximum operating temperatures during the

adjustment process and the desired operating temperature. The stabilization time is defined as the adjustment process time. The temperature deviation is defined as the difference between the steady-state operating temperatures after the adjustment process and the desired operating temperature. A detailed comparison of the two topologies under steady working conditions is shown in Table 2. Results show that the temperature overshoot of the distributed topology is larger than that of the integrated topology, while the stabilization time of the distributed topology is shorter than that of the integrated topology. This means that when the MFCS operates under steady working conditions, the integrated topology is superior in operating temperature control accuracy, while the distributed topology is superior in the adjustment process.

Table 2. The detailed comparison of the two topologies under steady working conditions.

Parameter	Distributed Topology			Integrated Topology		
	Stack1	Stack2	Stack3	Stack1	Stack2	Stack3
Temperature overshoot (K)	0.836	0.983	0.978	0.371	0.484	0.397
Stabilization time (s)	100	50	50	>300	>300	>300
Temperature deviation (K)	−0.077	0.04	−0.058	-	-	-

4.2. Variable Working Conditions

The three stacks' temperatures of the two topologies when the MFCS operates under variable working conditions are shown in Figure 17a,b. On the one hand, the operating temperature fluctuation of the distributed topology is obvious, and its range is −1~0.8 K. Operating temperature deviations in the three stacks are minimal. The operating temperature response of this topology is fast because each stack is separately controlled. On the other hand, the operating temperature fluctuation of the integrated topology is relatively moderate, and its range is −1 ~ 1.5 K. Operating temperature deviations in the three stacks are large. The operating temperature response of this topology is slow because the coordinate control is adopted among the stacks.

A detailed comparison of the two topologies under variable working conditions is shown in Table 3. Results show that the operating temperature difference of the distributed topology is smaller than that of the integrated topology. This means that when the MFCS operates under variable working conditions, the distributed topology is superior in operating temperature control accuracy because the operating temperature of each stack is controlled independently.

(a)

Figure 17. *Cont.*

(**b**)
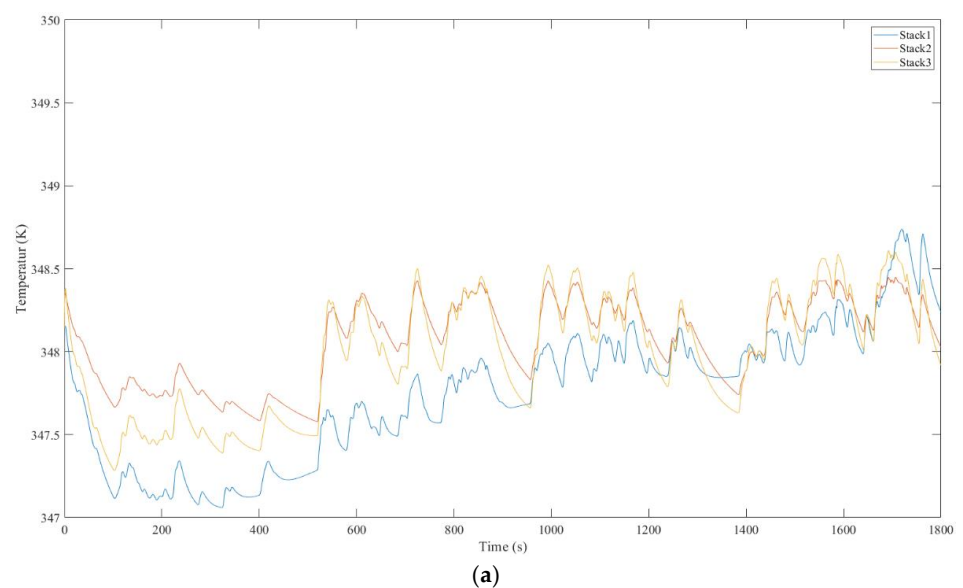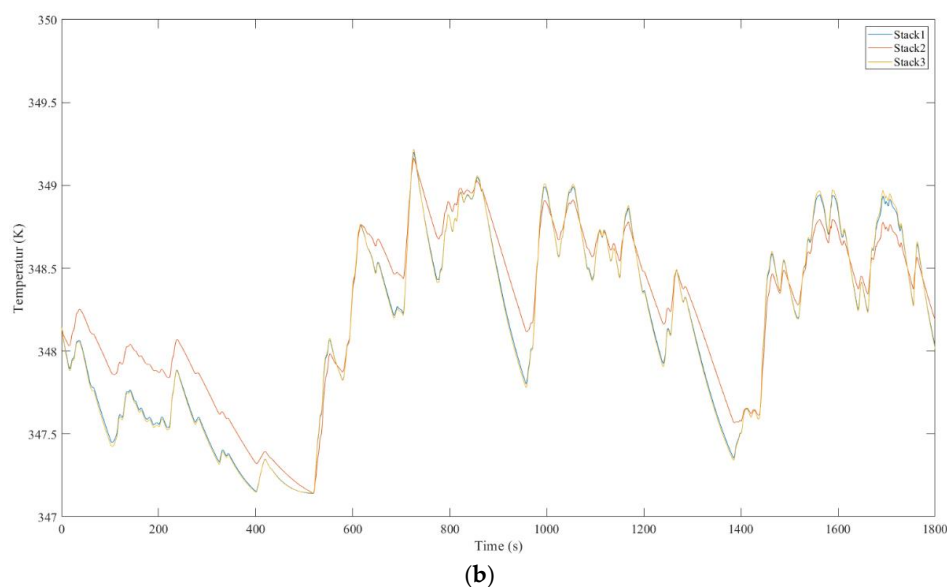
Figure 17. Three stacks' temperatures of the two topologies under variable working conditions: (**a**) distributed topology and (**b**) integrated topology.

Table 3. The detailed comparison of the two topologies under variable working conditions.

Parameter	Distributed Topology			Integrated Topology		
	Stack1	Stack2	Stack3	Stack1	Stack2	Stack3
Maximum temperature (K)	348.738	348.45	348.611	349.2	349.165	349.218
Minimum temperature (K)	347.061	347.577	347.283	347.142	347.143	347.144
Temperature difference (K)	1.677	0.873	1.328	2.058	2.022	2.074

5. Conclusions

This paper compares the stability duration and deviation of the operating temperature between the distributed and integrated topologies of the MFCS. Detailed conclusions are as follows:

(1) There are two topologies of the MFCS thermal management subsystem: the distributed and integrated topologies.

(2) When the MFCS operates under steady working conditions, the integrated topology is superior in operating temperature control accuracy ($\Delta T < 0.5$ K), while the distributed topology is superior in the adjustment process ($t \leq 100$ s).

(3) When the MFCS operates under variable working conditions, the distributed topology is superior in operating temperature control accuracy.

Author Contributions: W.S.: Conceptualization, Software, Writing—original draft, Project administration. L.F.: Software, Writing—original draft, Project administration, Formal analysis. Z.P.: Methodology, Software. C.C.: Validation, Data curation. N.W.: Funding acquisition, Resources, Supervision. S.Z.: Conceptualization, Methodology, Writing—review and editing, Funding acquisition, Supervision. All authors have read and agreed to the published version of the manuscript.

References

1. Liu, Y.; Pei, P. Asymptotic analysis on autoignition and explosion limits of hydrogen–oxygen mixtures in homogeneous systems. *Int. J. Hydrogen Energy* **2006**, *31*, 639–647. [CrossRef]
2. Liu, Y.; Fan, L.; Pei, P.; Yao, S.; Wang, F. Asymptotic analysis for the inlet relative humidity effects on the performance of proton exchange membrane fuel cell. *Appl. Energy* **2018**, *213*, 573–584. [CrossRef]
3. Li, Y.; Pei, P.; Ma, Z.; Ren, P.; Huang, H. Method for system parameter identification and controller parameter tuning for super-twisting sliding mode control in proton exchange membrane fuel cell system. *Energy Convers. Manag.* **2021**, *243*, 114370. [CrossRef]
4. Li, Y.H.; Pei, P.C.; Ma, Z.; Ren, P.; Huang, H. Analysis of air compression, progress of compressor and control for optimal energy efficiency in proton exchange membrane fuel cell. *Renew. Sust. Energy Rev.* **2020**, *133*, 110304–110324. [CrossRef]
5. Zhou, S.; Fan, L.; Zhang, G.; Gao, J.; Lu, Y.; Zhao, P.; Wen, C.; Shi, L.; Hu, Z. A review on proton exchange membrane multi-stack fuel cell systems: Architecture, performance, and power management. *Appl. Energy* **2022**, *310*, 118555. [CrossRef]
6. Zhou, S.; Zhang, G.; Fan, L.; Gao, J.; Pei, F. Scenario-oriented stacks allocation optimization for multi-stack fuel cell systems. *Appl. Energy* **2022**, *308*, 118328. [CrossRef]
7. Hirpara, V.; Patel, V.; Zhang, Y.; Anderson, R.; Zhu, N.; Zhang, L. Investigating the effect of operating temperature on dynamic behavior of droplets for proton exchange membrane fuel cells. *Int. J. Hydrogen Energy* **2020**, *45*, 14145–14155. [CrossRef]
8. Wu, D.; Li, K.; Gao, Y.; Yin, C.; Song, Y.; Yang, X.; Tang, H. Experimental and modeling study on dynamic characteristics of a 65 kW dual-stack proton exchange membrane fuel cell system during start-up operation. *J. Power Source* **2021**, *481*, 229115–229128. [CrossRef]
9. Départure, C.; Boulon, L.; Sicard, P.; Fournier, M. Simulation model of a multi-stack fuel cell system. In Proceedings of the 2013 15th European Conference on Power Electronics and Applications (EPE), Lille, France, 2–6 September 2013; pp. 1–10.
10. Mohamed Ramadan, H.S.; Bortoli, Q.; Becherif, M.; Claude, F. Multi-stack fuel cell efficiency enhancement based on thermal management. *IET Electr. Syst. Transp.* **2017**, *7*, 65–73. [CrossRef]
11. De Bortoli, Q.; Becherif, M.; Ramadan, H.S.; Boulon, L.; Claude, F. Thermal management for efficiency enhancement for multi-stack fuel cell electric vehicle. In Proceedings of the 2015 IEEE Vehicle Power and Propulsion Conference (VPPC), Montreal, QC, Canada, 19–22 October 2015.